Enhanced lithium battery cathode performance via mechanical grinding of CFx_MnO2 hybrid materials for space-grade applications: Unveiling synergistic effects

Louise Dauga, Guillaume Haddad, Dominique Foix, Delphine Flahaut, Diane Delbègue, Yannick Borthomieu, Bernard Simon, Marc Dubois, K. Guérin

Enhanced Lithium Battery Cathode Performance via Mechanical Grinding of CFx_MnO_2 Hybrid Materials for Space-Grade Applications: Unveiling Synergistic Effects

Louise Dauga[a], Guillaume Haddad[a], Dominique Foix[b], Delphine Flahaut[b], Diane Delbègue[c], Yannick Borthomieu [d], Bernard Simon[e], Marc Dubois[a,*], Katia Guérin [a,*]

[a] *Université Clermont Auvergne, CNRS, Institut de Chimie de Clermont-Ferrand, 63000 Clermont-Ferrand, France*

[b] *IPREM, Université de Pau et des Pays de l'Adour, E2S-UPPA, CNRS, 64053, Pau, France*

[c] *Centre National des Etudes Spatiales, 18 Avenue Edouard Belin, 31401, Toulouse, France*

[d] *SAFT, Space and Defense Division BP 1039, 86060 Poitiers, France*

[e] *SAFT, Direction de la recherche, 111-113 Bd A. Daney, 33074, Bordeaux, France*

* *Corresponding authors*

***Pr. Marc Dubois**

Professor (Head of « Inorganic materials » team) Université Clermont Auvergne, Institut de Chimie de Clermont-Ferrand (ICCF), 24 avenue Blaise Pascal, TSA 60026 CS 60026, 63178 AUBIERE Cedex, France.

Email: marc.dubois@uca.fr

Contact No. Office: +33473407105

ORCID Id: 0000-0002-9192-0931

*** Dr. Katia Guérin**

Associate Professor (Head of group: Fluorine Chemistry and Fluorinated Materials) Université Clermont Auvergne, Institut de Chimie de Clermont-Ferrand (ICCF), 24 avenue Blaise Pascal, TSA 60026 CS 60026, 63178 AUBIERE Cedex, France.

Email: Katia.araujo_da_silva@uca.fr

Contact No. Office: +33473407567

ORCID Id: 0000-0002-6184-2143

Abstract

CFx_MnO_2 hybrid cathode materials are prepared from a (C_2F)n-type graphite fluoride (CFx) and industrial MnO_2. Because of its physicochemical (insulating behavior, low content of CF_2 and CF_3 groups, no or a few remaining sp^2 carbon atoms) and electrochemical properties (flat plateau on galvanostatic curve and theoretical capacity of 623 mAh/g, higher than other conventional cathodes for primary lithium battery), graphite fluoride of $(C_2F)_n$-type is selected to evidence synergetic effects with MnO_2 that occur at the fluoride/oxide and electrolyte/ electrode interfaces. Both materials are mixed by mechanical ball-milling using different sets of parameters. The hybrid material presents very good electrochemical properties with a maximum energy density of about 1600 Wh per kg of active material. Notably, it shows a considerable improvement in voltage plateau and voltage delay compared to CFx. The parameters applied during ball-milling also shape the electrochemical performance of the new hybrid material. Ball milling increases the average discharge voltage plateau, and the power density of the battery, and avoids ohmic drop which may cause a battery to be eliminated as soon as it begins to discharge. More finely, electrochemical impedance spectroscopy shows that pushed grinding leads to more homogeneous but more polarized material-electrolyte interfaces so better diffusion and capacity but lower discharge potential.

Keywords : Lithium primary batteries, Carbon Fluorides, Manganese dioxide, hybrid materials, ball-milling, energy density

1. Introduction

Industrial applications for primary lithium batteries are developing rapidly in the fields of intelligent energy management, such as smart communicating meters, or vehicle fleet management, limiting greenhouse gas emissions. They also regard the space field and more particularly the energy management for space exploration applications when a solar array is not available to recharge a Li-ion battery [1]. In this case, manganese dioxide/fluorinated carbon MnO_2-CFx primary lithium battery PLBs could replace the conventional Li/$SOCl_2$ primary batteries which have been used for various exploration missions such as in Rosetta and its landers Philae and Mascot. It is therefore necessary to maximize both the energy density and the power of these systems as no handling can take place.

Li/CFx (atomic ratio F/C=1) have a theoretical capacity as high as 865 mAh/g. However, the electrical conductivity of CFx is very low due to the sp^3 hybridization of carbon involved in covalent C-F bonds [2], which leads to serious initial voltage delay at the beginning of the discharge along with low rate capability [3], inhibiting the use of CFx in high-power devices [4]. The preparation of sub-fluorinated graphite (F/C < 1, typically 0.7-0.8) was shown to be an effective approach to improve the rate capability of CFx because of the remaining non-fluorinated and conductive sp^2 carbons, allowing for easier electron transports within the material [5,6]. However, the specific capacity of CFx is decreased due to the lower F/C ratio (C-F bonds are the electroactive species). Other works [4] show that better-conducting properties can be achieved through the mechanical ball-milling of the CFx. To tackle to insulating property of CFx, it has been mixed with more conductive materials through coating or simply by preparing a composite material with carbon nanotube [7] conductive polymers [8] or oxides, notably $Ag_2V_4O_{11}$ [9], SiO_2 [10] and MnO_2 [11]. MnO_2 has shown to be a good candidate to mix with CFx as it has a good rate capability [12]. It can be found in different structures from 1D tunnel to layered or spinel-like structures. Most works use the γ-MnO_2 and β-MnO_2 for applications in PLBs [13]. It has a theoretical capacity of 308 mAh/g [13]. Cylindrical cells containing a hybrid cathode of CFx and MnO_2 have been manufactured by some companies such as Eagle Picher and Ultralife and show good

performance in comparison to Li/CFx cells. However, they still don't achieve the same performance as other technologies such as Li/$SOCl_2$ cells [1, 14]

Several works have tackled the association of CFx with MnO_2 through varying methods. A lot of them use the mixing of both materials in different proportions [15,16], hydrothermal synthesis can also be applied to obtain MnO_2 nanowires coating on CFx [17,19]. Some approaches consist of tuning the electrode arrangements to have both active materials working in the cell but without forming a composite of the two [20,21]. Several results have been noted through these studies. First of all, the association of CFx with MnO_2 provides better performance at higher current densities [18,20]. There is also a gain in voltage for these systems especially for materials containing between 20 wt% and 25 wt% of MnO_2 [15-18]. However, it is noted that sometimes, the resulting discharge curve for CFx_MnO_2 hybrid materials shows two distinct voltage plateaus, which can be a problem for the applications [18,22]. Among CFx families, the covalency of the C-F bond can be tuned owing to the precursors and the fluorination way. However, some improvements are needed both to adjust the discharge voltage of MnO_2 and CFx and avoid a bi-plateau [18,22].

Graphite fluoride can be described as a covalent fluorine-graphite intercalation compound (F-GIC). Among them, stage 2 with $(C_2F)_n$ structural type exhibits the highest discharge potential and flat galvanostatic discharge curve. The theoretical capacity of 623 mAh/g for $CF_{0.5}$ composition is higher than other conventional cathodes for PLB, e.g. 400 mAh/g for thionyl chloride $SOCl_2$. Because it is synthesized at a lower temperature in pure molecular fluorine gas (F_2), i.e. 400-450°C, it contains a lower amount of CF_2 and CF_3 groups. Located on the fluorocarbon sheet edges, those laters have a detrimental effect on the discharge mechanism. $(C_2F)n$ phase is an intermediate before the achievement of (CF)n graphite fluoride (stage 1 with FCF/FCF stacking). Because of the reactivity of F_2 gas, it is difficult to obtain the pure stage 2; it is often present either with graphite or with (CF)n phase (or both when the fluorination duration is too short at high temperatures). In a perfect $(C_2F)n$ phase with FCCF/FCCF stacking, half the carbon atoms are fluorinated, the other half exhibit sp^3 hybridization, and

the materials are then insulated. Because of those structural and electrochemical properties, stage 2 $(C_2F)n$ appears as a perfect material to evidence a synergetic effect with MnO_2 that enhances the performance as a cathode in PLB. If (CF)n or sub-fluorinated carbon with composition $CF_{0.8}$ [8] is used, the effects of the MnO_2/CFx interface could be masked or attenuated because of the presence of CF_2/CF_3 groups and sp^2 C, respectively. The discharge mechanism, which involves the formation of LiF from F^- and Li^+ions coming, respectively, from the electroreduction of C-F bonds and electrolyte, occurs at the sheet edges. Because CF_2 groups are present at this location, their influence is important although they are present in low amounts.

In this work, a quasi-perfect $(C_2F)n$ graphite fluoride was synthesized and mixed with β-MnO_2 through mechanical ball-milling to favor the intimacy of both phases. To discriminate the impact of ball-milling and that of the addition of MnO_2, the obtained hybrid material is compared, not only with the pristine CFx but also with the ball-milled CFx. It is shown how this particular phase with F/C around 0.5 and high structural homogeneity, which has a significantly different electrochemical behavior than commercially purchased CFx, impacts the performance of a CFx_MnO_2 hybrid material.

Experimental

1.1.Preparation of CFx_MnO_2 hybrid material and Materials Characterization

The graphite fluoride (CFx) was prepared from a Timrex KS44 graphite through a direct fluorination process using pure gaseous molecular fluorine F_2. A static mode was used to perform the fluorination for 72 h. 1 bar of F_2 gas was maintained in a closed reactor by the addition of F_2 to compensate for the pressure decrease due to the covalent intercalation of fluorine atoms. The reaction temperature was first maintained at 450°C for 24 h to form the $(C_2F)n$ phase and then increased to 610°C as annealing to increase the structural homogeneity [23]. After the fluorination and during the cooling of the reactor, the reactive atmosphere was flushed with nitrogen gas. The weight uptake evidences a F/C molar ratio of

0.60 for the fluorinated graphite, slightly higher than the value expected for the $(C_2F)n$ phase (F/C = 0.50). This is the first indication of the preparation of a majoritary $(C_2F)n$ phase. The MnO_2 was provided by SAFT company and has a particle size of 40 µm. The hybrid CFx-MnO_2 material was obtained through mechanical ball-milling in an 80:20 weight ratio. We used a design of experiments (DOE) pilot through an experiment plan to determine the best sets of parameters during ball-milling in between grinding duration and grinding speed. In this work, we will present two materials: one for which the materials were mixed at 250 rpm for 8 hours (HBM for hard ball-milling) and one for which they were mixed at 450 rpm for 1 hour (SBM for soft ball-milling). The CFx was ball-milled with the same parameters as HBM for comparison. Hard and soft refer to changes induced by ball-milling, i.e. drastic or moderated, respectively, see thereafter.

Powder X-ray diffraction (XRD) patterns were obtained using a PANalyticalXpert Pro diffractometer equipped with a CuKα1 source and analyzed using X'PertHighSore Plus Software. Scanning electron microscopy (SEM) images were acquired on an FEI Nova NanoSEM 450 FE-SEM. ^{19}F and ^{13}C solid-state nuclear magnetic resonance (NMR) spectra were acquired on a Bruker AVANCE spectrometer. 2.5 mm zirconia rotors rotating at 30kHz were used. For MAS spectra, a simple sequence was performed with a single $\pi/2$ pulse length of 4.0 and 3.5 µs for ^{19}F and ^{13}C, respectively. ^{13}C NMR was performed at a frequency of 73.4 MHz and tetramethylsilane (TMS) was used as the reference. ^{19}F NMR was carried out with a frequency of 282.2 MHz and the spectra were externally referenced to $CFCl_3$.

Fourier-transform infrared (FTIR) spectra were recorded on a Nicolet 6700 FT-IR (Thermo scientific) spectrometer in transmission mode at 4 cm^{-1} resolution and 256 scans were taken for each spectrum.

Electronic Paramagnetic Resonance (EPR) spectra were acquired with a Bruker ER041XG in X-band (9.85 GHz) at a power of 0.0217 mW. Typically, 5mg of powder was poured into a quartz tube under air. The parameters (received gain, modulation, power) were optimized both to avoid saturation and

maximize the signal/noise ratio. The EPR signals were normalized by the weight of the sample and then fitted with two derived Lorentzian curves and an affine baseline correction.

X-ray photoemission spectroscopy (XPS) measurements were carried out with a THERMO Escalab spectrometer, using focused monochromatic Al Kα radiation (hν = 1486.6 eV) and equipped with an argon-filled glove box allowing to preserve the samples from moisture and air at all times from their preparation to their analysis. Peaks were recorded with a constant pass energy of 20 eV. The pressure in the analysis chamber was around 2×10^{-7} mbar and the analyses were done using charge compensation. The binding energy scale was calibrated using the C 1s peak at 285.0 eV associated with the CH_2-carbons from hydrocarbonated contamination present at the surface of the samples. The spectra were fitted using a minimum number of components. Several spectra were recorded at different times to check that the samples were not subjected to degradation during the X-ray irradiation.

1.2. Preparation of CFx_MnO_2 electrodes, cell assembly, and Electrochemical Characterization

Active material (HBM, SBM, CFx, HBM-CFx, and MnO_2), polyvinylidene difluoride (PVDF from Aldrich), and acetylene black (from Mersen) were mixed with an 80:10:10 weight ratio, and stirred vigorously in N-methyl-2-pyrrolidinone (NMP) to form a slurry. This slurry was cast on an aluminum foil using a doctor blade. The cast was then dried at 80°C. The electrodes had a loading of about 2 mg/cm² (single side) and were then punched into 13mm disks and transferred into a glove box in an argon atmosphere for cell assembly. Three Celgard separators impregnated with the electrolyte 1M LiTFSI in EC :PC: DMC (1 :1 :3, %vol.) were placed between the electrodes and a lithium foil was used both as counter and reference electrode. The button cells (CR2032) were assembled in an argon-filled dried glove box.

The electrochemical performance was evaluated at room temperature and measurements were carried out on a VMP3 or a BCS Biologic instrument. Relaxation was performed for 5h or 8h depending on the material until the open circuit voltage (OCV) was stabilized. Three to five coin cells were made for each

material to ensure the reproducibility of the results on almost 3 coin cells. Galvanostatic discharges were carried out between 1.5V and 4.1V with a C/80 current rate (1C = 687 mAh/g for CFx and HBM-CFx; 1C = 308 mAh/g for MnO_2, 1C=611 mAh/g for HBM and SBM). The specific capacity is calculated considering both CFx and MnO_2 as the active material, according to their weight fraction in the material. The high rate performance was evaluated by applying currents from C/80 to C/2 regimes according to the demands of the application. The Electrochemical Impedance Spectroscopy (EIS) was performed by applying a signal with an amplitude of 5mV between 0.01Hz and 100kHz. The cyclic voltammetry was performed from the open circuit voltage of the cell to 2V. The scanning rate of 0.0009 mV/s was applied. All voltage data will be referenced vs. Li^+/Li.

2. Results and discussion

2.1.Physico-chemical characterizations of the hybrid materials

The structures of HBM and SBM CFx_MnO_2 hybrid materials have been characterized by XRD and compared to MnO_2, CFx, and CFx milled in the same conditions as HBM (denoted HBM-CFx); the corresponding patterns are shown in Fig. 1. CFx exhibits typical peaks corresponding to the (001) and the (100) planes of a fluorocarbon lattice at 2Θ equal to 9°62 and 41°, respectively. The peak corresponding to the (001) plane evidences an interlayer distance of 9Å, which corresponds to a $(C_2F)n$ stage 2 covalent F-GIC. The FCCF/FCCF stacking sequence in the $(C_2F)n$ phase results in a higher d_{001} than 6Å for stage 1 (CF)n with CF_1 composition and (FCF/FCF stacking sequence)[24]. The interlayer distance unambiguously indicates a majority $(C_2F)n$ phase. Nevertheless, the XRD peak must be fitted with two components centred at 8.9° (interlayer of 9Å) and 12° (7.4Å) (Fig. S1) that evidences the presence of (CF)n too, with 23%. The interlayer distance of the second component is not 6Å as expected for pure (CF)n phase but 7.4Å. This second component is mainly (CF)n but distorted by the presence of majority $(C_2F)n$. As seen by XRD, the long-range order appears as largely predominant stage 2, i.e. $(C_2F)n$ phase, in the material as it represents about 77% of the signal. Because fluorination is a heterogeneous gas/solid reaction, one may reasonably expect that the majority $(C_2F)n$ phase is

surrounded by the $(CF)_n$-like phase (nearly saturated with F atoms)[24]. The absence of a peak at 26° evidences that no sp^2 hybridized carbon crystalline region is left from raw graphite. The pattern of HBM-CFx exhibits nearly the same features as the raw CFx, suggesting slight structural changes due to mechanical ball-milling. The peak is slightly broader with a full width at half maximum of 3.66° (3.48° for raw CFx). The percentages of (C_2F)n and (CF)n are not changed by milling. The results also show that the MnO_2 is a mixture of δ-phase and β-phase which is consistent with MnO_2 commonly used for electrochemical applications [25]. On both hybrid materials, all the peaks can be attributed to either CFx or MnO_2. The ball-milling does not affect the ratio of phases(C_2F)n/(CF)n. Moreover, MnO_2 structure is not affected by mechanical grinding certainly because the hardness of MnO_2 is higher than those of (CF)x phases.

[FIGURE 1 GOES HERE]

Solid-state ^{19}F NMR spectra with the spinning rate of 30 kHz of HBM and SBM CFx_MnO_2 hybrids show three distinct ^{19}F species as for raw CFx and HBM-CFx (Fig. 2a). Both peaks at -186 ppm and -175 ppm correspond to C(sp^3)-C-F related to the (C_2F)n phase; the two chemical shifts are related to different neighborings, i.e. C-F in (C_2F)n and (CF)n, respectively [26]. Interaction of C-F bonds with residual sp^2 carbons results in the shoulder at -80 ppm. Its low intensity reveals that the relative content of sp^2 C is weak, in agreement with the XRD analysis; even at short range, as seen by NMR, this conclusion is valid. The signal at -116 ppm is related to CF_2 groups located at the edges of the carbon layers. By fitting this signal, it appears that the proportion of CF_2 groups in HBM-CFx, HBM, and SBM is slightly lower than in CFx. Fluorine atoms in those groups are those which are primarily impacted during mechanical milling as they are located on sheet edges and may be decomposed to release fluorine

atoms. Those data are corroborated by Infrared spectroscopy measurements (Fig. S2). Infrared spectra of HBM and SBM appear as a superimposition of the signal for HBM-CFx and MnO_2.

Solid-state ^{13}C NMR (Fig. 2b) is in agreement with XRD and confirms both the absence of sp^2 hybridized carbon atoms in the samples (line expected at 130-140 ppm) and the formation of $(C_2F)n$ as the main structural type; the line at 42 ppm is assigned to non-fluorinated sp^3 C atoms that are then exclusive for $(C_2F)n$-type [26]. The second main line is related to covalent C-F bonds, with similar chemical shifts (84 ppm) whatever the structural phase $(C_2F)n$ or (CF)n. Fit of the spectra allows the ratio of phase contents to be extracted. According to the area of the lines $S_{C\text{-}F}$ and S_{Csp3}, the ratio $(C_2F)n/(CF)n = 100\ S_{Csp3}/S_{C\text{-}F}$ (perfect $(C_2F)n$ phases must exhibit ^{13}C NMR spectrum, respectively, with $S_{Csp3} = S_{C\text{-}F}$ and $S_{Csp2} = 0$). 75% of C-F bonds are included in the $(C_2F)n$-type (25% in (CF)n) whatever the sample (which is consistent with XRD data). In other words, the $(C_2F)n$ phase represents 75% of the fluorocarbon lattice. Moreover, the F/C ratio remains constant at 0.60 regardless of the presence of MnO_2 and ball-milling. The fitting of the signals which allows the determination of the F/C ratio is shown in Fig. S3.

[FIGURE 2 GOES HERE]

MnO_2 is a paramagnetic compound (Mn^{4+} ion configuration is $[Ar]3d^3$) and acts in the nuclear relaxation (reduce the relaxation times) of ^{19}F nuclei (and ^{13}C thereafter). The paramagnetic neighboring enlarges the lines whatever the nucleus ^{13}C or ^{19}F; this results in the appearance of spinning sidebands (marked with asterisks in Fig. 2). Fits including the spinning sidebands give the same $(C_2F)n/(CF)n$ than for the isotropic lines evidencing that paramagnetic Mn^{4+} ions are close enough to affect the resonances of all magnetic ^{13}C and ^{19}F.

The characterization techniques which probe the bulk of the materials, either at long (XRD) or short range (NMR and IR) reveal that the ball-millings maintain the properties in terms of a high percentage

of $(C_2F)n$ phase (75%), low C sp^2 content and C-F bonding (covalent). Moreover, the ball-millings allow homogeneous dispersion of MnO_2 and CFx to be achieved.

Techniques which probe the surface and morphology were also used to reveal differences between HBM and SBM hybrids. SEM images of single materials and both hybrid materials are shown in Fig 3. The CFx particles exhibit the typical layer stacking structure of F-GIC and the above particle size is around 40 µm. After ball-milling without MnO_2, it is noticeable that the layer structure of graphite is modified, showing that the process has an impact on the homogeneity of the material. The MnO_2 particles are irregular with a range of particle sizes centered around 40 µm. The hybrid materials exhibit different nanostructures and it is difficult to differentiate CFx and MnO_2 parts after ball-milling. In the case of HBM-CFx, the layered structure of F-GIC has completely disappeared. The same conditions of ball-milling with MnO_2 result in the same effects on the fluorocarbon lattice for the hybrid HBM whereas it is still visible in SBM. It appears that the time of ball milling has a more significant impact on the texture of the material than the speed of rotation. The total loss of the lamellar structure of CFx explains the notation chosen for HBM (hard ball-milling) contrary to SBM (some lamellar grains are visible in Fig. 3e).

[FIGURE 3 GOES HERE]

Fig. 4 shows the energy dispersive X-ray spectroscopy (EDX) elemental mapping of HBM and SBM. Whatever the milled sample, fluorine atoms are perfectly located on the carbon sites and not on the manganese sites. At this scale, there is no apparent manganese-fluorine bonding, i.e. transfer of fluorine from CFx to MnO_2.

[FIGURE 4 GOES HERE]

X-ray photoelectron spectroscopy (XPS) led to information on the chemical state and environment of manganese, carbon, and fluorine in MnO_2, ball-milled MnO_2, CFx, HBM-CFx and both hybrid materials HBM and SBM. Fig. 5 shows the C_{1s}, $Mn_{2p,}$ and F_{1s} spectra. The C_{1s} spectra (Fig. 5a) for the MnO_2 samples correspond only to surface contamination. For the 4 other samples, these spectra are fitted through three different components associated with three environments of carbon species at a binding energy of 290.3 eV for C-F, 291.8 eV for CF_2, and 288.5 eV for sp^3 carbon atoms with fluorinated neighboring, which are indicative of the $(C_2F)n$ phase. As observed by XRD, the absence of a carbon peak at 284.6 eV characteristic of sp^2 carbon shows that almost all the carbon atoms are fluorinated and that no raw graphitic region exists. As shown in Fig 5a, the grinding of CFx leads to a decrease of the CF_2 groups and an increase of the $(C_2F)n$ at the surface of the material. Through grinding, the core with $(C_2F)n$ phase appears at the surface and is then better detected by XPS for the ground samples. An opposite behavior is found for CF_2 groups, the intensities of their lines are maximal on the surface of non-ground grains, and new surfaces without CF_2 are created by ball-milling and analyzed by XPS. The carbon spectra for the hybrid materials are very similar to the pure ground CFx, with a higher proportion of carbon at 285.0 eV from hydrocarbonated contamination coming from MnO_2.

The Mn_{2p} spectra (Fig. 5b) for MnO_2 are characteristic of Mn^{4+} species in an oxide environment [27]. After milling, no change in shape and position of spectra is observed, linked to the hardness of this material as discussed earlier through XRD results. For hybrid materials, the Mn_{2p} spectra are similar for both HBM and SBM. Compared to the reference MnO_2, a global shift towards higher binding energy is observed as highlighted by the superimposed image, linked to the electronegativity induced by the presence of an important amount of fluorine. But no change in the oxidation degree and bonds is observed. The observation of F_{1s} spectra (Fig. 5c) can confirm this observation. Indeed, its peak position around 688.5 eV, for all the CFx and hybrid materials, is indicative of C-F bonds and excludes any Mn-F or Mn-O-F bonds. These XPS results confirm the observations provided by the other characterization techniques concerning the C-F bonding and the homogenous dispersion of MnO_2 and CFx in the hybrid

materials. Nevertheless, the nature of the phase and chemical composition on the surface has changed. More, $(C_2F)n$ layers and fewer CF_2 groups are present at the outmost surface.

[FIGURE 5 GOES HERE]

Electron paramagnetic resonance was used to investigate the defects in the materials and oxidation state of manganese. The signals of all materials are shown in Fig. 6. For CFx, the signal is assigned to dangling bonds (DB), and its linewidth is related to their fluorinated environment [29]. The linewidth of the signal is 17 G and the g factor is 2.003+/-0.001 in good accordance with the literature [29]. For the MnO_2 component, a nearly symmetric line with a g factor of 1.994+/-0.001 is observed. Its peak-to-peak linewidth (ΔHpp) is 3526 G. The difference in the linewidths with CFx allows the signals to be discriminated. A comparison of the signals of HBM, SBM, CFx, HBM-CFx, and MnO_2 evidences two things. Firstly, the area of the CFx signal is decreased in both hybrid materials and then the density of DB is lowered. Secondly, the width of the MnO_2 signal is greatly reduced, going from 3600 G to approximately 300 G. As revealed by XPS data, MnO_2 is surrounded by a fluorocarbon phase that results in a strong interaction between the two components [28]. The narrowing of the Mn^{4+} signal is related to a dilution effect by the fluorocarbon lattice that decreases the magnetic interaction between Mn^{4+} ions.

Even if the bulk properties are not changed, investigations at the outmost surface and morphology reveal that the nature of the phase and chemical composition are changed: i) More $(C_2F)n$ layers are on the surface with fewer CF_2 groups, ii) thanks to a homogeneous dispersion, MnO_2 and CFx strongly interact iii) the ball-milling may result in different morphologies with no (HBM) or residual lamellar grains (SBM). All these characteristics may affect the electrochemical properties by changing the interphase with the electrolyte.

[FIGURE 6 GOES HERE]

2.2. Electrochemical properties

The galvanostatic discharge curves of CFx, MnO_2, ball-milled CFx and both hybrid materials are shown in Fig. 7a. The discharge current at C/80 is calculated owing to the following theoretical values representative of C regime (CFx: 687 mAh/g for F/C = 0.60; MnO_2: 308 mAh/g; HBM-CFx: 687 mAh/g, Hybrid Materials: 611 mAh/g). The specific capacity of CFx is 93% of the theoretical specific capacity whereas the one of MnO_2 is only 76% because of either a two high current density or the presence of δ-phase. The start of the discharge shows the typical voltage delay that is expected for fluorinated graphite. It is due to the insulating property of CFx. Its voltage plateau is well-defined at 2.39V, which is classical for a $(C_2F)n$ phase [30]. This shape confirms the high homogeneity of the second stage F-GIC. The voltage plateau registered for MnO_2 at 2.80V is by the literature [14]. While the ball-milling did not impact the specific capacity of CFx, it is noticeable that the voltage plateau was increased to 2.47V for ball-milled CFx. The voltage delay at the beginning of the discharge is also greatly improved by ball-milling alone. Such improvements could be explained by the presence of conductive sp^2 carbon atoms on the surface but neither XPS nor NMR data evidence those atoms in an amount high enough to act. The presence of $(C_2F)n$ layers and fewer CF_2 groups may explain the enhancements. CF_2 groups are located on the sheet edges where both the exchanges of Li^+/F^- occur and LiF is formed. Their presence results in an additional resistance that decreases the discharge potential.

Even though CFx and MnO_2 show different voltage plateaus (separated by 0.4 V), both hybrid materials exhibit a single voltage plateau that is highly desirable for the application. According to the discharge curves of HBM and SBM, it is notable that adding MnO_2 to CFx changes the electrochemical performance. Both hybrid materials show a significant improvement in the voltage plateau (+0.08V for HBM vs. CFx) and (+0.19V for SBM vs. CFx). It demonstrates the synergistic effect of co-grinding. Most notably, the voltage delay, which was very apparent in CFx, was greatly reduced in both hybrid materials (Fig. 7b). It constitutes also another proof of the synergistic effect. This could be explained by the fact that by adding MnO_2 to the active material, the conductivity of the electrode was increased. It

can also noted that the discharge curves of the hybrid materials show relatively different profiles. While SBM shows the highest gain in potential, it delivers 532 mAh/g which is 87% of the calculated theoretical specific capacity for the CFx_MnO_2 hybrid material. On the other hand, HBM exhibits a specific capacity of 587 mAh/g but the uptake in potential is less significant. The excess in capacity obtained can be related to MnO_2 being electrochemically active and taking part in the discharge process. These differences between the two hybrid materials come solely from different parameters used during mechanical milling that change the morphology of the grains. This evidences that adapting these parameters is key to manufacturing the material with the best performance either energy for high favored capacity or power for high favored voltage. The contribution of MnO_2 is highlighted by plotting the curves only considering CFx as the active material. The curves are shown in Fig S4. The considered theoretical capacity is that of CFx only (675 mAh/g). For both HBM and SBM, it is noted that the capacity obtained largely exceeds the theoretical capacity, meaning that the reduction of C-F bonds is not the only electrochemical process during discharge. This points to MnO_2 acting as not only a conductive additive but also as part of the electrochemical process, despite its characteristic voltage plateau (2.80V) not being apparent. Cyclic voltammetry which is presented in Fig. S5 is in perfect accordance with galvanostatic data concerning the discharge potential. Indeed, the main and unique reduction peak of HBM and SBM is centered at a potential resulting from a synergistic effect of MnO_2 reduction and ground CFx (HBM_CFx). This potential is neither the potential of raw MnO_2 (higher) nor the one of the ground material (lower). One more time, grinding appears as a good way to enhance the average discharge potential of a CFx material. SBM grinding conditions favor a more centered potential peak and the consecutive higher discharge plateau through galvanostatic mode.

[FIGURE 7 GOES HERE]

The galvanostatic discharge curves of CFx, MnO2, HBM, and SBM at different current rates are presented in Fig. 8. The average discharge voltage ($E_{1/2}$) measured at half discharge capacity, the discharge capacities (Q), obtained for these materials are presented in Table S1. The CFx exhibits poor

rate capacity for higher current than C/10, the voltage delay at the beginning of the discharge takes the cell below the 2V cut-off. This is following literature showing CFx materials have poor rate capacity [17]. As for MnO_2, it exhibits an important loss of performance as the discharge capacity at C/2 is 40 mAh/g. For both materials, the increase of the current density leads to a decrease in this discharge voltage but remains at acceptable values for the application. Both HBM and SBM exhibit similar electrochemical profiles at low rates like C/80 and C/40. However, the average voltage plateau is higher for SBM whereas the capacity is higher for HBM. For HBM material, its higher voltage compared to CFx allows for HBM material to work at higher current densities such as C/4 and C/2 whereas it was impossible for CFx. However, there is a significant drop in capacity and voltage from C/10, while SBM maintains a capacity of 356 mAh/g (58% of the theoretical capacity) and a voltage plateau of 2.28V at C/2. Finally, SBM has a power density of 696 W/kg higher than the raw CFx 152 W/kg or HBM (617 W/kg), or even MnO_2 (337 W/kg). This highlights how the ball-milling process parameters influence the electrochemical performance of the material as HBM and SBM exhibit widely different behaviors at higher current densities. Out of the two materials, SBM is the one that has the best high-rate performance as it retains a satisfying capacity while increasing the average voltage compared to CFx. To fully understand the origin of the higher capacity of HBM and higher voltage of SBM a deeper electrochemical characterization is needed.

[FIGURE 8 GOES HERE]

The spectra from EIS of CFx, MnO_2, ball-milled CFx, HBM, and SBM and their equivalent circuit are shown in Fig. 9. The equivalent model was chosen from the work described in ref [31]. It can be noted that the model has encased interfaces and that is still the case with the addition of another interphase with MnO_2. The electrolytic resistance (R1) was significantly decreased after mixing the CFx with MnO_2 which is consistent with the great reduction in voltage delay for hybrid materials. The R1 value for ball-milled CFx (HBM-CFx) shows that the electrolytic resistance was also greatly reduced by

mechanical milling alone, although not as much as when MnO_2 is present. This corroborates what is observed during the discharge, as ball-milled CFx exhibits a reduced voltage delay compared to pristine CFx but this is more improved by the addition of MnO_2. The first loop (R2 and Q1) indicates the phenomenon on the surface of the cathode while the second loop (R3, Q2, M2) gives information on the diffusion mechanism in the bulk. R1 reflects the basic ohmic resistance of the cell. Q1 is related to the charge accumulation at the surface of the material. Ball-milled CFx and HBM have a lower Q1 value than CFx. This is explained by the fact that mechanical milling harmonizes the inhomogeneous nature of the surface in CFx, more $(C_2F)n$ and less CF_2 are present on the surface making it more favorable for diffusion. All the physicochemical characterizations evidenced the homogeneity of the HBM hybrid, in good accordance with physico-chemical characterization. On the other hand, SBM shows a much higher value for Q1, meaning there is a surface inhomogeneity in this material by the maintaining of the lamellar shape at the micrometric scale (Fig. 3). This leads to a restricted diffusion within the material which can be demonstrated by the higher R3 value for SBM and explains its lower capacity. Q2 also indicates the diffusion within the cathode. The higher its value is, the higher the voltage delay that decreases the operating potential of the battery. The fact that Q2 is considerably lower for SBM is consistent with its discharge curve where both a 0.30V gain in potential and no potential delay were achieved. This means that it is possible to predict the behavior of a material during discharge by looking at the Q2 value. EIS is therefore an interesting method for pre-diagnosis of a cell. A combination of EIS data and physicochemical multi-scale characterization is powerful in explaining the enhancement or decrease of electrochemical properties.

Table 1 Values of the parameters obtained by simulation of EIS spectra

	R1 (Ω)	R2 (Ω)	R3 (Ω)	Q1 (F)	Q2 (F)	χ^2
CFx	30	69	14	43E-06	2E-03	12.99
HBM	10	32	23	36E-06	5E-03	5.264
SBM	1	34	38	467 E-06	8E-06	17.49
MnO_2	24	72	3E+12	1E-05	4E-06.	11.18
HBM-CFx	14	74	40	23E-6	3E-03	27.12

[FIGURE 9 GOES HERE]

3. Conclusion

In this work, CFx_MnO_2 materials usable as cathodes of primary lithium batteries have been prepared. An almost homogenous $(C_2F)n$ phase was used as the CFx phase to favor the starting from a homogenous phase before the grinding. Ball-milling is an efficient way to achieve a synergy between both materials and the performance of the battery can be modulated by adapting the parameters for the mechanical ball-milling. While structural modifications have not been observed, surface characterization techniques show that the process influences heavily the phase located on the surface and the morphology of the material. Gas/solid fluorination results in fluorine saturation on the surface of the grain with the presence of CF_2 groups and (CF)n layers (CF_1). During milling, the $(C_2F)n$ core without CF_2 groups is exposed to the surface and covered with MnO_2 for the case of the hybrid. CFx/MnO_2 and CFx/electrolyte interphases are changed thanks to the homogeneous mixing at the nanometric scale for HBM and the micrometric scale for SBM. Such interfaces result in a unique voltage plateau that addresses higher power densities (four times the value of an unground material) with either high voltage or high capacity values which can be interesting for applicative purposes. The main advantage of adding MnO_2 is to reduce the ohmic drop and the resulting voltage delay. The use of electrochemical impedance

spectroscopy is also shown to be a reliable method of pre-diagnosis of a cell regarding its voltage and the way to understand the modification of electrolyte/electrode material interface. Other kinds of nanostructured oxides such as CuO or Mn_3O_4 can be synergetically mixed by the same methodology with CFx to go further on increased power densities.

References

[1] F.C. Krause, High Specific Energy Lithium Primary Batteries as Power Sources for Deep Space Exploration, J. Electrochem Soc, 165 (2018) A2312.

[2] D. Wang, G. Wang, M. Zhang, Y. Cui, J. Yu, S. Shie, Composite cathode materials for next generations lithium fluorinated carbon primary batteries, J. Power Sources, 541 (2022) 231716.

[3] Z. Fang, Y. Peng, X. Zhou, L. Zhu, Y. Wang, X. Dong, Y. Xia, Fluorinated carbon materials and the applications in energy storage systems, Applied Energy Materials, 5 (2022) 3966.

[4] M.A. Reddy, B. Breitung, M. Fichtner, Improving the energy density and power density of CFx by mechanical milling: a primary lithium battery electrode, Applied Mater. Interfaces, 5 (2013) 11207.

[5] K. Guérin, M. Dubois, A. Houdayer, A. Hamwi, Applicative performances of fluorinated carbons through fluorination routes: a review, J. Fluor. Chem., 134 (2012) 11.

[6] J. Giraudet, C. Delabarre, K. Guérin, M. Dubois, Comparative performances for primary lithium batteries of some covalent and semi-covalent graphite fluoride, J. Power Sources, 158 (2006) 1365.

[7] Y. Li, Y.F. Chen, W. Feng, F. Ding, X.J. Liu, The improved discharge performance of Li/CFx batteries by using multi-walled carbon nanotubes as conductive additive, J. Power Sources,196 (2011) 2246.

[8] H. Groult, C.M. Julien, A. Bahloul, S. Leclerc, E. Briot, A. Mauger, Improvements of the electrochemical features of graphite fluorides in primary lithium battery by electrodeposition of polypyrrols, Electrochem. Com., 13 (2011) 1074.

[9] P. Meduri, H. Chen, X. Chen, J. Xiao, M.E. Gross, T.J.Carlson, J-G.Zhang, Z.D. Deng, Hybrid CFx-$Ag_2V_4O_{11}$ as a high-energy, power density cathode for application in an underwater acoustic microtransmitter, Electrochem. Com., 13 (2011) 1344.

[10] Y. Zhu, L. Zhang, H. Zhao, Y. Fu, Significantly improved electrochemical performance of CFx promoted by SiO_2 modification for primary lithium batteries, J. Mater. Chem. A, 5 (2017) 796.

[11] A. D. Pathak, S. Saha, V.K. Bharti, M.M. Giwad, C.S. Sharma, A review on battery technology for space application, J. Energy Storage, 2 (2023) 106792.

[12] N. Sharma, M. Dubois, K. Guérin, V. Pischedda, S. Radescu, Fluorinated (Nano)Carbons: CFx Electrodes and CFx- based Batteries, Energy Technology, 9 (4) (2021) 2000605

[13] J. Shin, J.K. Seo, R. Yaylian, A. Huang, Y. S. Meng, A review on mechanistic understanding of MnO2 in aqueous electrolyte for electrical energy storage systems, Inter. Mater. Reviews, 65 (2019) 1.

[14] J.W. Marple, Performance Characteristics of Li/MnO_2-CFx Hybrid Cathode Jellyroll cells, J. Power Sources, 19 (1987) 325.

[15] Y. Chang, M. Wang, S. Wang, J. Na, A. Bund, A. K. Nanjundan, Y. Yamauchi, Ultralong storage life of Li/MnO_2 primary batteries using MnO_2-(CFx)n with semi-ionic bond as cathode materials, Electrochimica Acta, 320 (2019) 134618.

[16] K. Yang, Z. Shan, X. Liu, M. Dong, J. Tian, S. Wang, Study on modifying the Li/MnO_2 battery by mixing with carbon fluorides, Energy Storage, 2 (2020) 128.

[17] Z. Luo, J. Wan, W. Lei, Y. Zhao, Y. Pan, Z. Ma, A simple strategy to synthesize CFx@MnO2 nanowires composite cathode materials for high energy density and high power density primary lithium batteries, Mater. Tech., 35 (2020) 836.

[18] K. Yang, Z. Shan, X. Liu, S. Wang, Effect of MnO_2 on expansion force inhibition and electrical proporties of Li/CFx battery, Mater. Lett., 309 (2022) 131421.

[19] L. Li, R. Wu, H. Ma, B. Cheng, S. Rao, S. Lin, C. Xu, L.Li, Y.Ding, L. Mai, Towards the high-performance lithium primary batteries by chemically modified fluorinate carbon with δ-MnO2, Small, 19 (2023) 2300762.

[20] Y. Li, W. Feng, The tunable electrochemical performances of carbon fluorides/manganese dioxide hybrid cathodes by their arrangements, J. Power Sources, 274 (2015) 1292.

[21] P.C. Latorre, T.B. Atwater, An analysis of hybridization methods and techniques for CF-MnO_2 blends, 49th Power Sources conference, 2022.

[22] Y. Chang, M. Wang, S. Wang, J. Na, A. Bund, A.K Nanjundan, Y. Yamauchi, Ultralongstorage life of Li/MnO_2 primary batteries using MnO_2-(CFx)n with C-F semi-ionic bond as cathode materials, Electrochimica Acta, 320 (2019) 134618.

[23] N. Watanabe, Two Types of graphite fluorides, (CF)n and (C_2F)n, and discharges characteristics and mechanisms of electrodes of (CF)n and (C_2F)n in lithium batteries, Solid State Ionics, 1 (1980) 87.

[24] Y. Kita, N. Watanabe, Y. Fujii, Chemical composition and crystal structure of graphite fluoride, J. Am. Chem.l Soc., 101 (1979) 3832.

[25] A. Biswal, B.C.Tripathy, K. Sanjay, T. Subbai, M. Minakshi, Electrolytic manganese dioxide (EMD): a perspective on worldwide production, reserves and its role in electrochemistry, RSC Adv., 5 (2015) 58255.

[26] W. Zhang, M. Dubois, K. Guérin, A. Hamwi, J. Giraudet, F. Masin, Solid-state NMR and EPR study of fluorinated carbon nanofibers, J. Solid State Electrochem., 181 (2008) 1915.

[27] E.S. Ilton, J.E. Post, P. J. Heaney, F. T. Ling, S.N. Kerisit, XPS determination of Mn oxidation states un Mn (hydr)oxides, Applied Surface Science, 366 (2016) 475.

[28] A. Biswal, B.C Tripathy, T. Subbaiah, D. Meyrick, M. Minakshi, Electrodeposition of manganese dioxide : effect of quarternary amines, J. Solid State Electrochem., 17 (2013) 1349.

[29] M. Kakazey, N. Ivanova, Y. Boldurev, S. Ivanov, G. Sokolsky, J.G Gonzalez-Rodriguez, M. Vlasova, Electron paramagnetic resonance in MnO_2 powders and comparative estimation of electroc

characteristics of power sources based on them in the MnO_2-Zn system, J. Power Sources, 225 (2003) 170.

[30] T. Nakajima, R. Hagiwara, K. Moriya, N. Watanabe, discharge characterisctics of poly(carbon monofluoride) prepared from the residual carbon obtained by thermal decomposition of poly(dicarbon monofluoride) and graphite oxide, J. Electrochem. Soc., 133 (1986) 1761.

[31] M. Mathews, Advancing Li/CFx Battery Chemistry: a study on partially reduced CFx as a primary Li/CFx cell cathode material (2011). Theses and Dissertations. 406.

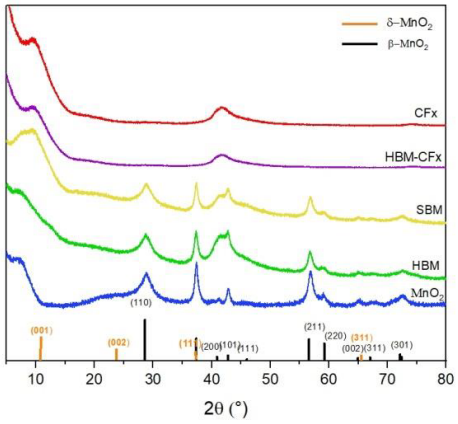

Figure 1 : XRD patterns for all materials

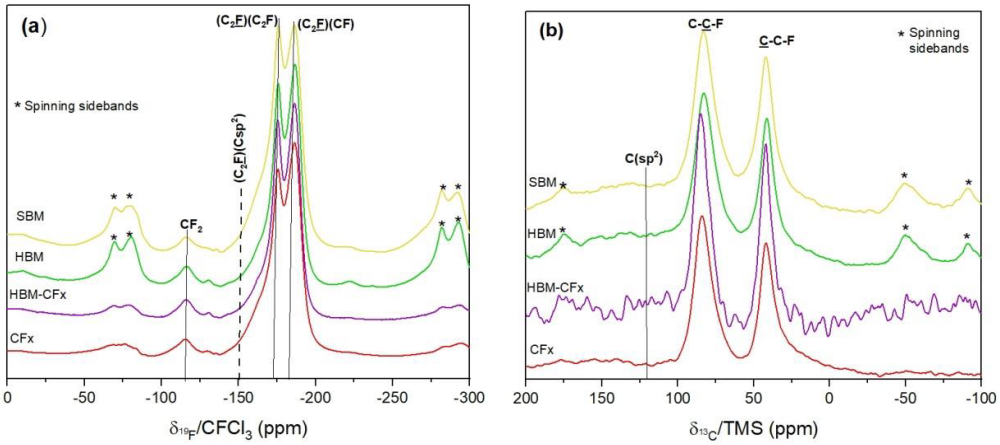

Figure 2 : ^{19}F (a) and ^{13}C (b) solid-state NMR spectra of CFx (red), HBM-CFx (purple), HBM (green) and SBM (yellow)

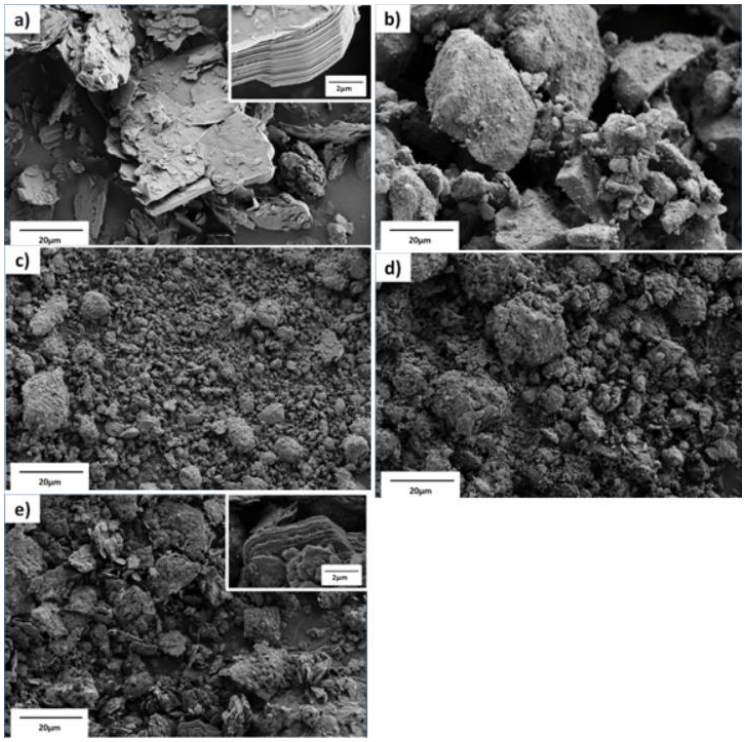

Figure 3 : SEM images for a) CFx b) MnO_2 c) HBM-CFx, d) HBM, e) SBM

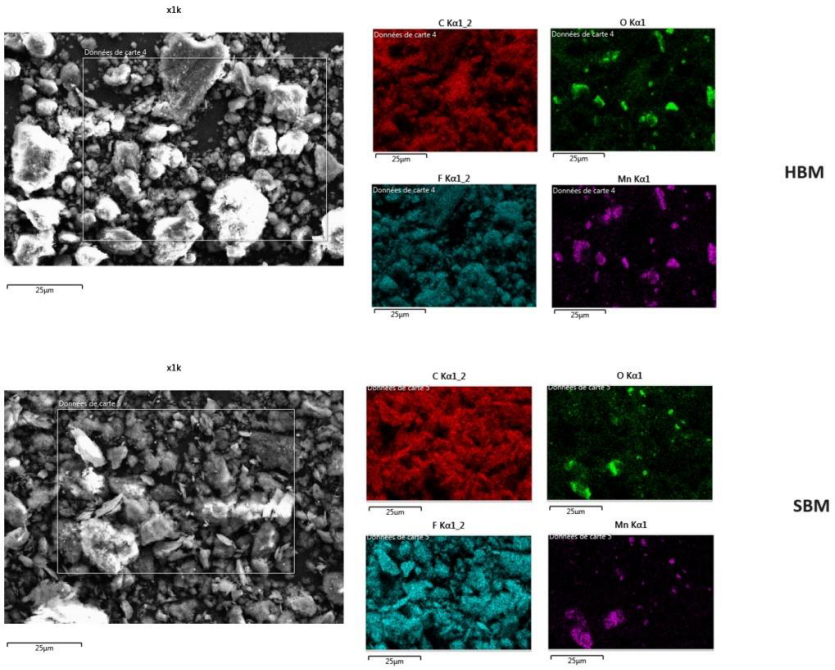

Figure 4 : EDX images for HBM and SBM

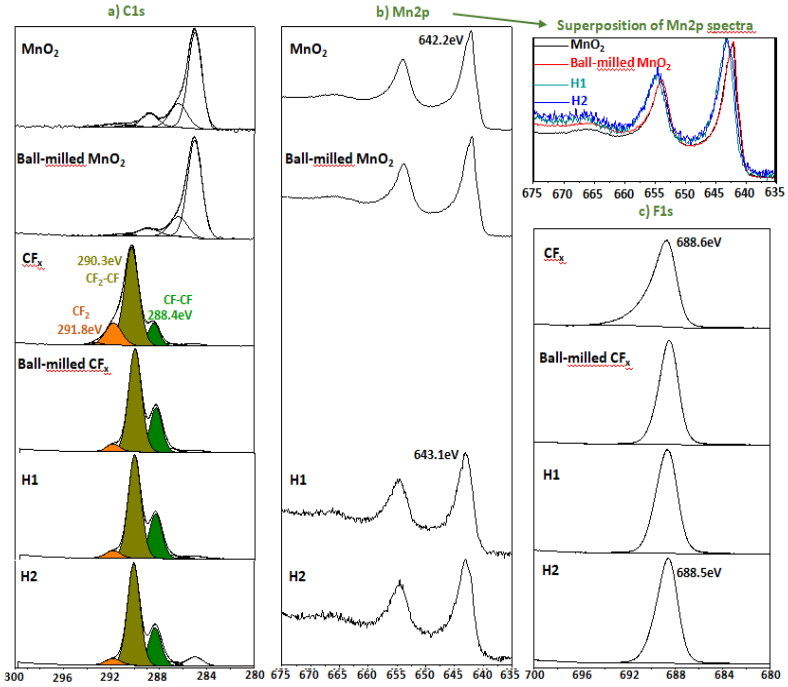

Figure 5 : a) C1s, b) Mn2p and c) F1s XPS spectra

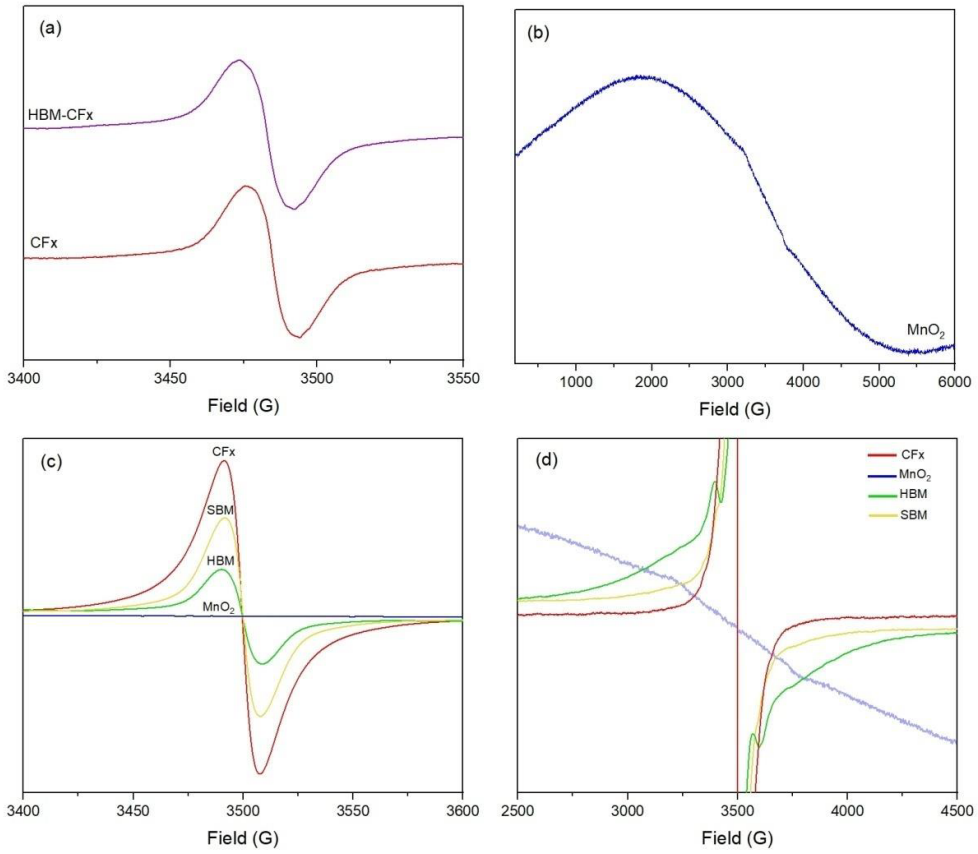

Figure 6 : EPR spectra for all materials

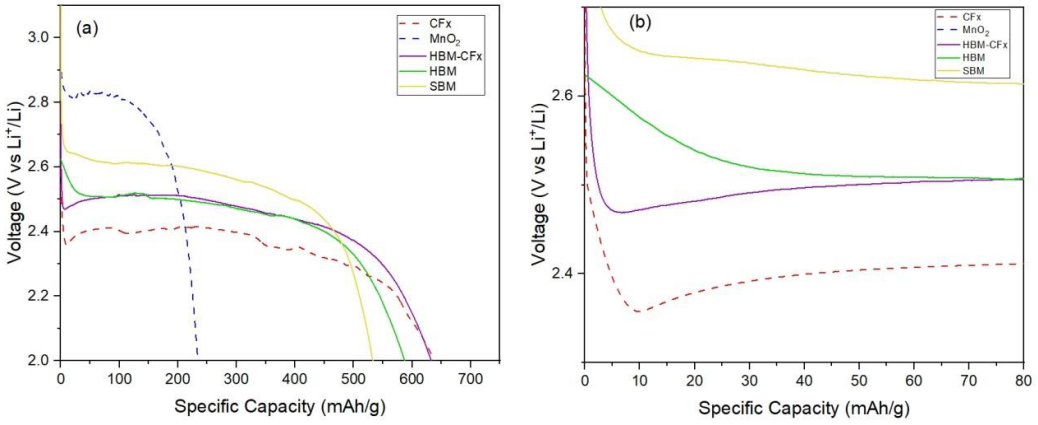

Figure7: Discharge curves at C/80 of CFx (dotted red), MnO_2 (dotted blue), HBM-CFx (purple), HBM (green), SBM (yellow)// LiTFSI 1M PC/EC/3DMC // Li

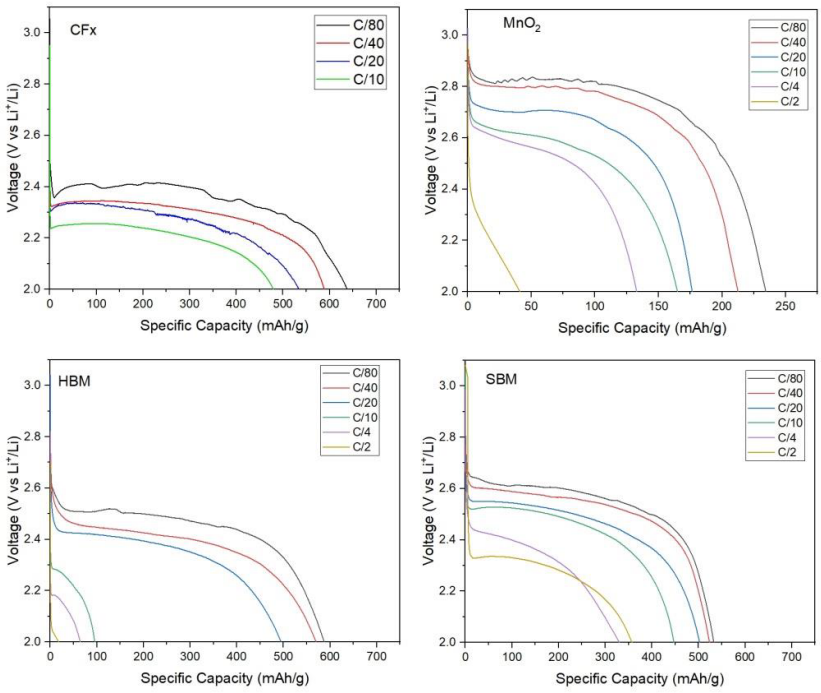

Figure 8: Discharge curves at various current densities of CFx (red), MnO_2 (blue), HBM-CFx (purple), HBM (green), SBM (yellow)// LiTFSI 1M PC/EC/3DMC // Li

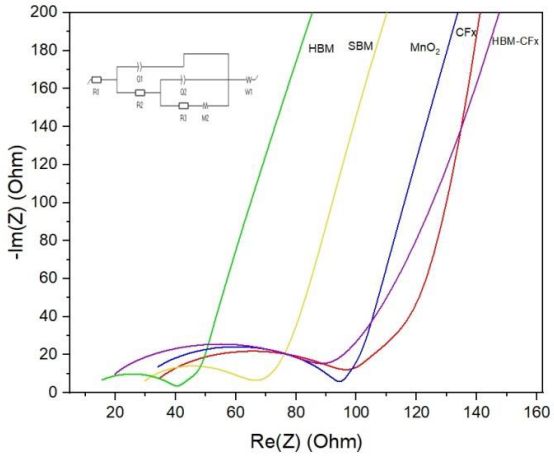

Figure 9: EIS spectra of CFx (red), MnO_2 (blue), HBM-CFx (purple) HBM (green) and SBM (yellow) electrodes and the equivalent circuit used in inset